Mechanisms of nucleation and defect growth in undercooled melt containing oxide clusters

Sepideh Kavousi and Mohsen Asle Zaeem*

Department of Mechanical Engineering, Colorado School of Mines, Golden, CO 80401, USA

Abstract

Mechanisms governing the nucleation and defect growth during solidification of undercooled aluminum (Al) in the presence of oxide clusters are studied by molecular dynamics (MD) simulations. Without serving as heterogeneous nucleation sites or changing the overall average grain size, Al oxides (Al_2O_3) induce localized variations in nanostructures away from the oxide surfaces. Thermodynamic modeling of solidification based on the terrace-ledge model suggests that the non-wetting nature of the liquid Al- solid Al_2O_3 interface prevents formation of perfect and twinned structures on oxide surfaces. Delayed crystal nucleation and steady-state solidification followed by a sharp growth of smaller grains are identified to trigger variations in crystal orientation selection and increase the localized fraction of twinned structures in regions between oxide surfaces. Finally, our investigation of formation of growth twin boundaries provides the first computational evidence that both layer-by-layer additions and formation-decomposition of grain boundaries mechanisms govern the formation of five-fold twin boundaries during solidification of Al.

Keywords: Solidification; Aluminum oxide; Nanostructure heterogeneity; Growth twins; Molecular dynamics.

*Corresponding author: zaeem@mines.edu (M. Asle Zaeem)

1. Introduction

Alloys containing aluminum (Al) have a large affinity for oxygen and formation of Al oxides (mainly Al_2O_3) [1]. When the surface of melt goes under turbulence flow during the pouring process, an oxide layer can also fold over itself with entrapped air within and this is called an oxide bifilm. The presence of oxide bifilms in the material affects the mechanical properties of products made through melting and solidification (e.g., casting) [1-5] and has a profound impact on the manufacturing of safety-critical components [3, 6-9]. Bifilm defects have a major role in degrading the quality and reliability of castings [1-5, 10]. Formation of volumetric defects (such as pores and cracks) in castable alloys is mostly process-related and affected by oxide bifilms. Accordingly, many studies in the literature focused on identifying the environmental, material, and microstructural factors that reduce the amount of oxidation in materials by changing processing parameters, such as cooling rate [11], melt stirring [12, 13], velocity of melt entering [13, 14], and mold filling direction [8, 15, 16], as well as the alloy composition [17, 18]. While these studies provide valuable insights into the oxidation problem, commercial manufacturing of alloys free from bifilms does not exist at this time [19, 20]. Thus, the detrimental effects of the oxides and oxide bifilms on the mechanical properties of the material cannot be eliminated unless we have a clear understanding of the origination, evolution, and properties of oxides and oxide bifilms and their impacts on different stages of solidification.

A few studies [21, 22] reported that the oxide films act as proper sites for heterogeneous nucleation and can be used for refining grains in alloys containing Al. While others suggested that the nonmetallic inclusions, such as oxides, are mainly non-wettable particles and thus unfavorable nucleation sites for solidification [23-25]. Therefore, they do not believe oxide skins are favorable nucleation sites [10, 26] unless for intermetallic phases [19, 27, 28] growing on the outer and wetted surfaces of bifilms. There is not sufficient evidence that the grain refinement or microstructure heterogenies is associated with the initiation of heterogenous nucleation from the oxide surfaces [22]. Understanding formation and evolution of microstructures in the vicinity of an oxide layer during the initial stages of crystal nucleation is needed to uncover the mechanisms governing the microstructure heterogeneities during solidification of metal melts containing oxides. In this paper, we will address this knowledge gap by investigating the possibilities of

both homogenous nucleation inside the undercooled melt and heterogenous nucleation from the oxide surfaces.

The localized refinement of grains is known to alter microstructural features, such as defects growing during the solidification. There are few studies that observed a high fraction of twin boundaries (TBs) inside refined microstructures [29-31]. However, the reason for this high fraction of TBs inside the refined microstructures is not yet understood. In order to control the growth of twins and the final microstructures, we first need to unravel the formation mechanisms of these twins.

TBs are low-energy planar defects that can improve the strength of nanocrystalline materials without compromising their ductility or electric conductivity [32]. For materials with higher stacking fault energies, such as nickel and aluminum [33], the formation of nano-twinned structures is more difficult than for those with lower stacking fault energies, like copper [34] and stainless steel [35]. However, some experimental [36, 37] and atomistic studies [38-40] reported formation of 5-fold TBs in high stacking fault energy materials. TBs are mainly categorized into two groups. The first one is the growth twins that are formed during the non-equilibrium material processing and require growth incidents during the liquid to solid transformation (i.e., solidification). The second group is the deformation twins, which accommodate strain in plastic deformation [41, 42]. Different studies observed the formation and evolution of both 5-fold [43] and lamellar [44] twins during a highly stressed deformation process of nickel-chromium-molybdenum alloy and nanocrystalline Al, respectively. However, there are very limited studies focused on the formation and evolution of growth TBs during the solidification process. A high fraction of TBs was observed in solidified Al-Zn [29], pure Al [31], and Au–Cu–Ag [30] with small amounts of Cr (0.1 wt%), Ti (0.2 wt%), and Ir (0.01 wt%), respectively. Grain refinement was attributed to the growth of icosahedral quasicrystals (iQC). However, they still could not explain why the grain refinement is accompanied by the increase in TB fraction.

The lack of available experimental equipment for monitoring the nuclei formation had been limiting our current understanding of nanostructure evolution and defect formation during different stages of solidification. Recent advances in this field have come through numerical simulation techniques such as molecular dynamics (MD) [39, 40]. The goal of this study is to advance our understanding of how oxide bifilms affect the phase nucleation and formation of

twinned structures during different stages of solidification. For this purpose, we perform MD simulations of solidification of Al containing different numbers of Al_2O_3 clusters. By investigating the localized variations of grain orientations, TB fraction, and grain size, we aim to determine the mechanisms governing both the nucleation, defect formation, and nanostructure evolution during solidification.

2. Methodology

2.1. Molecular dynamics simulations

We perform MD simulations to investigate how the oxides affect the nanostructure evolution and defect formation at various stages of solidification. The simulation starts by melting a system consisting of ~1.6 M Al atoms. Starting from a face-centered cubic (fcc) structure with periodic boundary conditions in all three directions, the simulation system is first melted by increasing the temperature to 1500 K under a constant number-volume-temperature (NVT) ensemble for 20 ps. Then the system is equilibrated at the melting point (924.9 K) for 200 ps by performing a constant number-pressure-temperature (NPT) ensemble by applying a Nose-Hoover thermostat and barostat. The calculated melt density at the melting point is 2436 kg/m^3 which is close to the experimental value of 2375 kg/m^3 [45]. Later, the isothermal solidification condition is imposed on the simulation system by performing NPT, with P and T set to 0 atm and 500 K, respectively. The solidification simulations are completed for three different systems. The first one includes solidification of pure Al with no oxide (Al-NO). The second and third ones study the solidification of Al with one oxide (Al-OO) layer, and three oxide (Al-TO) layers, respectively. The size of each oxide layer is 100×100×12 Å^3, and for Al-TO, we distribute the three layers with equal spacing along the y-direction. Each case (Al-No, Al-OO, and Al-TO) is simulated twice. Each independent solidification simulation has been performed utilizing the same SL coexistence at the melting point as the initial condition. Random seed numbers are chosen in thermostat settings to replicate independent MD simulations through a different initial velocity distribution in the system. Each of the system replicas has a fixed overall temperature of all the atoms, but a different set of velocities for atoms on each processor. This ensures that each simulation is independent. It should be noted that each MD simulation performed in this study used on average 400,000 CPU hours and repeating the solidification simulation several times to

obtain the uncertainties is computationally expensive. Bootstrapping is a good alternative method for obtaining uncertainty quantification at a reasonable computational cost. In general, bootstrapping involves resampling with replacement from the available data to create fictional datasets, called bootstrap replicates [46, 47]. In this study, each bootstrap replica is a random re-occurrence of the crystal structure choice for each atom in the system. This method is used to quantify the uncertainties pertaining to the time evolution of the phase fractions during solidification. The size of each replica equals the number of atoms in the simulation system, and once we had 400 system replicas for each time frame, we used them to obtain the mean and standard deviation for the phase fraction variations.

The interatomic potential used to describe the atomic interactions in Al is the 2NN-MEAM potential developed by Mahata et al. [45]. This interatomic potential presents accurate predictions of the high-temperature thermophysical properties such as melting point (924.9 K [45]) and enthalpy of fusion (11.5 kJ/mol [45]). The interatomic potential used for predicting the interactions between the Al-O in aluminum oxide is an in-house MEAM+Qeq interatomic potential which will be presented in a separate manuscript. This potential is tested for different properties of the Al oxide phases and charge distribution and presents the charge neutrality in the regions near the Al and oxygen. The use of MEAM+Qeq interatomic potential requires using a very small timestep equal to 0.0005 ps. All the MD simulations are performed using LAMMPS (Large-scale Atomic/Molecular Massively Parallel Simulator developed by the Sandia National Laboratories) [48]. Post-processing is performed via various modifiers and python scripting platform embedded in Ovito [49].

2.2. Developing post processing codes

In crystallography, the orientation of a grain can be represented by either a rotation axis and angle, or a matrix. The first description can be used to identify the grains in body-centered cubic (bcc) structures, and when the rotation angle between two atoms is smaller than a threshold [50], the atoms belong to the same grain. However, this definition is not useful for the fcc systems, because the formation of TBs inside the fcc lattice will affect the rotation axes and angles. On the other hand, various atomic arrangements can result in formation of TBs. For instance, $\sum 3$ coherent grain boundary can form by either 60° twist around <111> or 70° tilt from

[110] on (111) plane. Both cases have the same atomic arrangement near a TB, which makes them structurally indistinguishable [51]. As an alternative, we propose a new technique in this study which is based on the matrix representation of each grain and the transformation matrix. Consider R_{G1} and R_{G2} to be the matrix representations for grains G1 and G2. Therefore, the matrix corresponding to the boundary between these grains (T_{12}), given by Equation (1), clarifies if the boundary is a TB and identifies its nature (twist, tilt, etc.) [52].

$$T_{12} = R_{G1}R_{G2}^{-1} \ . \qquad (1)$$

In this study, we used Python scripting embedded in Ovito to calculate the matrix representation to determine which atoms are associated with which phases and which are associated with defects. We developed a code based on the polyhedral template matching function [53] to classify structures according to the topology of their local atomic environment. This python code (presented in Supplementary Materials, Section 2) provides a thorough representation of the orientation of the nuclei growing inside the melt. The matrix representation helps obtaining the transformation matrix across any boundary inside the simulation system. Using this new approach in solidification studies will not only help identifying the nature of the boundary (Supplementary Materials, Section 5), but also result in obtaining a more accurate identification of grains in the final structure. This code provides all the required descriptors of the grain orientation: matrix, rotation matrix and angle, and the Euler angles. In order to identify the boundary characterization, we first calculate the rotation matrix for all the atoms inside a grain. Then, we calculate the matrix representation of the boundary using Eq (1). Comparing the boundary's representation matrix with the reference representations of various boundaries given in [51] helps identifying the boundary's characteristics. Using this method, we are able to make the first computational observations of grain refinement near oxide clusters, explain how it happens, and how it affects the growth of TB defects. This method has several advantages over previous ones used in post-processing of MD trajectories and is more reliable than common neighbor analysis in the presence of thermal fluctuations [53]; this model can I) be applied to study both bcc and fcc materials, II) accurately characterize TBs, III) identify homogenous nucleation from both the surface of the other grains and oxides, IV) accurately calculate grain numbers, and V) trace the uncommon phenomenon during the solidification.

Figure 1(a) shows a snapshot of the AL-TO simulation where the atoms are colored based on their rotational axes. Enlarged sections of two interesting nanostructural features designated by the green and blue rectangles are shown in Figure 1(b) and Figure 1(c). Investigating the matrix representations of grains, shown in Figure 1(b), helps us to identify the characteristics of the TBs formed at the intersections of G1, G2, and G3 grains with the central grain, G4. The matrix representation of grains can be obtained using the python code provided in the Section 2 of the Supplementary Material. For example, by analyzing the matrix representation of G1 and G4 grains, we can show that the matrix T_{14} between grains G1 and G4 corresponds to a TB formed via a -60° twist around <111> axis. Using a similar method, one can determine the formation of TB in between G2-G4 and G3-G4 with -60° twist around the $<11\bar{1}>$ and 70° twist tilt from $<\bar{1}\bar{1}0>$ axes, respectively.

In addition, the structural orientation definition enables us to uncover new features of the microstructure evolution during solidification. For instance, as shown in Figure 1(d), the shape of the probability distribution of grain angles suggests that there are a few grain orientations that are more favored during the solidification of Al. The probability distribution of the angle is calculated for the solidified system. Additional discussions about this are provided in the result section related to Figure *5*.

Based on the classical nucleation theory [54], when an embryo reaches a critical nucleus size, it grows into a cluster as it turns into a solid phase. Based on MD calculations (Supplemental Material Figure S1), the solid-liquid interface free energy based on capillary fluctuation method [55-58] for Al is 173 $\pm$ 2.3 mJ/m^2, which gives the critical nucleus diameter of approximately 1.7 nm. However, in a few incidences, such as the snapshot shown in Figure 1(c), the nucleus is overgrown by the neighboring nuclei and it starts dissolving into the melt. At t=126.75 ps, three nuclei (G5, G6, G7) are growing, which are all larger than the critical nuclei size predicted by the classical nucleation theory. Therefore, one might expect the continuous growth of all three nuclei during the solidification. However, as the nanostructure evolves, the nucleus G5 is overgrown by G6 and G7. Coloring based on the grain orientation clearly shows that G5 is melted and G6 and G7 grow larger. This phenomenon might be attributed to Ostwald Ripening [59, 60] which predicts the growth of larger clusters at the expense of smaller ones without direct contact between grains. This mechanism was investigated in various experiments

[61-63], MD simulations [64], and theoretical studies [64, 65] which mostly discussed the effects of grain sizes on the Ostwald Ripening process.

Ostwald ripening in multi-component systems is a result of diffusion of atoms from the small grains into the larger grains resulting in the dissolution of small ones. However, the Ostwald Ripening mechanism for pure materials is different. Kukushkin [66] proposed a hypothesis on Ostwald Ripening of a new phase nucleus during the crystallization of melt. For a pure material, the crystallization rate is determined by removal of the latent heat of crystallization from the growing nucleus into the melt and it depends on the thermal conductivity of melt. During the solidification of pure material, the "faceted" nuclei grow due to the layer-by-layer mechanism. Theoretical studies on single- and multi-component materials in the literature [64-66] ignore the effect of growth orientation and the texture of the solid phase in predicting the time evolution of nuclei radius. However, our previous works [67-70] emphasized the dependence of the SL interface energy on the interface orientation between solid and liquid, which questions the general conclusion of Oswald Ripening that having a larger/smaller radius will eventually lead to growth/shrinkage of adjacent nuclei. Results in Figure 1 (c) highlight the dependence of Oswald Ripening on the grain orientations, in addition to their sizes. In the example in Figure 1, G5 was not the smallest grain among the neighboring G5, G6, and G7 grains. Since the probability of having a rotation angle of 38° in the final nanostructure was very small, this grain melted as a result of Ostwald Ripening. Applying the new matrix representation as a tool for analyzing the clusters growing inside the melt helps us to pinpoint the dynamics of the ripening process and emphasize the importance of the orientation of grains, which was not observed previously.

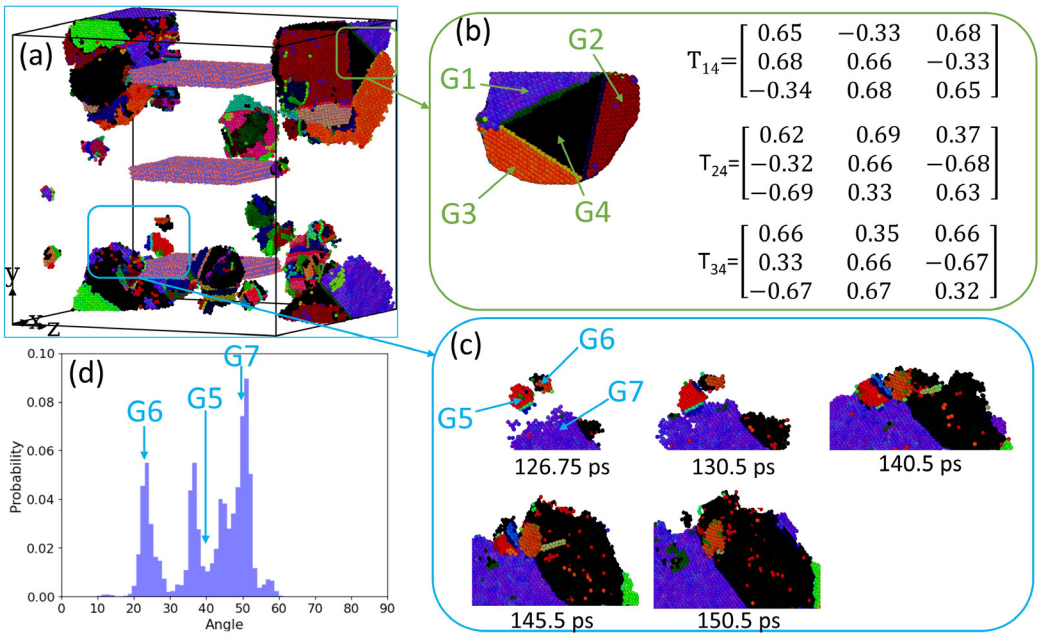

Figure 1. (a) Snapshot of simulation for the solidification of Al-TO. The coloring of atoms is based on the grain orientation, (b) the correlations for rotational matrix for TB formations, (c) melting of G5 during the growth of G6 and G7, and (d) the probability distribution of grain angle in the final nanostructure of AL-TO solidification. The orientation of G5, G6 and G7 are marked by arrows.

We developed additional python codes to determine the clusters and study the evolution of solidification nanostructures; these codes are presented in sections 3 and 4 in the Supplementary Material. We took an innovative approach to identify the stable clusters by introducing an order parameter. The order parameter value is determined based on the number of atoms with fcc or hcp crystal structures among the 14 first nearest-neighbor (1NN) and second nearest-neighbors (2NN) of each atom. The order parameter is zero unless the number of neighboring atoms with an fcc/hcp structure exceeds 7. In this case, the order parameter takes the value of one.

3. Results

3.1. Mechanisms governing nucleation and growth of nanograins

One of the important questions that is addressed in this paper is how the presence of oxides affects the initial nucleation stages of solidification. Some studies suggest that an oxide

surface may act as a preferred nucleation site for heterogeneous nucleation [21, 22]. While others [10, 26] suggest that the oxide layers do not promote the formation of heterogenous nuclei. Our MD simulation results support the second scenario. In the simulation with one oxide cluster, no grains nucleated from the surface of the oxide layer. And in the case of three oxide clusters, we identified only one small nucleus (marked as G8 in Figure 2b) formed on the surface of the oxide layers. We identify this as a heterogenous nucleus because it is formed in the vicinity of the surface, and the orientation relationship at the interface between nuclei and substrate is $Al(111)//Al_2O_3(0001)$, which matches the previous first principle calculations [71], MD simulations [72, 73] and experimental studies [74]. Despite this one heterogenous nucleus growing near the oxide surface, we still believe the oxide surface is not a favored nucleation site. As shown in Figure 2b, the variation in the number of grains along the y-direction does not present an increase in the number of grains in the vicinity of oxides. Instead, a large number of grains are formed in regions approximately halfway between neighboring oxides. Previous experimental [75] and simulation [75] investigations suggested that the nonwetting-wetting transition of liquid Al on α-$Al_2O_3(0001)$ would not take place unless the melt temperature is above 1000 K. This supports our conclusion that the oxide surfaces do not promote the formation of heterogenous nuclei. However, a large surface area/volume ratio of the oxide clusters may just slightly increase the tendency of grain nucleation in their vicinity.

The variation of nanostructures along the y-direction (see Figure 2(b)) suggests that the presence of oxides leads to an inhomogeneity in the distribution of grains in the nanostructure. However, the question is how the existing oxides inside the melt alter the average grain size and its variance. In this study, we used two methods to estimate the average grain size in the simulation system. First, we counted the number of final grains inside the simulation system. Despite the localized heterogeneity in grain distribution, the overall number of grains in the simulation system was almost the same. Having a final number of 23, 24, and 23 grains inside the simulation box gives the average grain size of 56.7 Å, 55.9Å, and 56.7Å for Al-NO, AL-OO, and AL-TO, respectively. Second, we sliced the simulation system along y-direction into bins with 10Å thickness and determined the average radius of grains. This method estimates the average grain size for Al-NO, Al-OO, and Al-TO to be 63.87 ± 2.7 Å, 64.35 ± 6.5 Å, and 63.53 ± 8.0 Å, respectively. Despite the small difference between the results of these two methods, it is clear that the average grain size does not change dramatically between three simulations.

However, the abundance of oxide clusters in the simulation system highly affects the variations of the grain size inside the simulation system. This denotes a significant heterogeneity in the distribution of grains for this case.

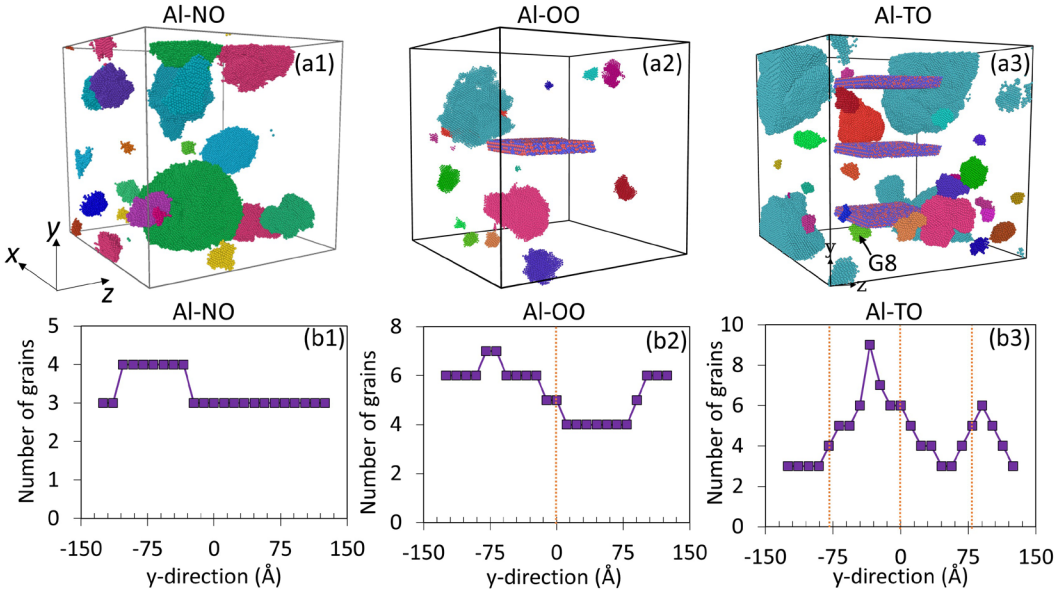

Figure 2. (a) The initial nuclei formed during solidification of (a1) no oxide (Al-NO), (a2) one oxide layer (Al-OO), and (a3) three oxide layers (Al-TO). (b) The variation of number of grains in the solidified nanostructure along the y-direction in (b1) Al-NO, (b2) Al-OO, and (b3) AL-TO. The dotted orange lines show the position of oxide layers in the simulation systems.

Additional analysis on the time evolution of crystal structures during solidification, presented in Figure 3, highlights the overall effect of oxides on the nucleation which is to delay the nucleation process. Results presented in Figure 3 are obtained by calculating the mean phase fraction of 200 bootstrap replications of each set of simulations (400 in total) at each time frame. However, the very large sample size results in having a very small standard deviation (maximum values of 0.2%, 0.18%, and 0.18% for Al-NO, Al-OO, and AL-TO, respectively). Therefore, we skipped presenting error bars in Figure 3. Details of the python code used for performing bootstrap replications are presented in section 4 of the Supplementary materials.

The initial structure corresponds mostly to the liquid phase. Over time, the system becomes more ordered, and fcc nuclei start to form during the solidification process. The initial stage is followed by a sharp increase in the fcc atoms. After the solidification is completed, fcc grains occupy almost the whole simulation domain. The rest of the atoms are distributed into the

available space, forming grain boundaries and defects such as TBs, stacking faults, and vacancies.

The nucleation process starts with small nuclei, which subsequently grow into spherical-like grains as their sizes surpass the critical nucleus size. In the case with no oxides, it took about 40 ps for the initial nucleation stage to complete, and the solid clusters that were formed inside the liquid phase started to grow into stable nuclei. The initial stage of nucleation for the cases with one and three oxide-clusters is determined to be ~45 ps and ~60 ps, respectively. This suggests that the oxide clusters delay the initial stage of the nucleation process. However, if the heterogenous nucleation was controlling the solidification process, the steady-state stage of the solidification, the region with almost linear time evolution of amorphous phase fraction (shown in Figure 3), should have started earlier.

By investigating the linear portion of amorphous fraction variations, we observed that the oxide clusters also affect the steady-state solidification stage. The steady state solidification rates of 9514 atoms/ps and 6101 atoms/ps for Al-NO and Al-TO simulations suggest that the steady-state solidification rate is much higher when the oxide clusters are not present inside the simulation box. The overall solidification time for the case with no oxide is 20% smaller than the case with three oxide layers. On the other hand, detailed analysis of fcc fraction variations in the purple window in Figure 3, denoting the simulation times between 200 ps and 300 ps, shows that a large portion of the Al-NO simulation system is solidified prior to time = 200 ps. While the oxide clusters delay the solidification growth and a huge portion of the fcc fraction increase (from 29% to 69%) takes place between 200 ps and 300 ps. Previously, we observed localized heterogeneity in the grain distribution of the AL-TO simulation system. The refined microstructure can be attributed to the delayed solidification followed by a sharp change of fcc fraction from 200 ps to 300 ps of the simulation time. In summary, although the overall solidification time for AL-NO was shorter than for AL-OO and AL-TO simulations, the delayed nucleation in the vicinity of oxide clusters, resulted in a localized refinement of grains near the oxide clusters. There are some experimental studies supporting our results by showing grain refinements where the probability of heterogenous nucleation is low [10].

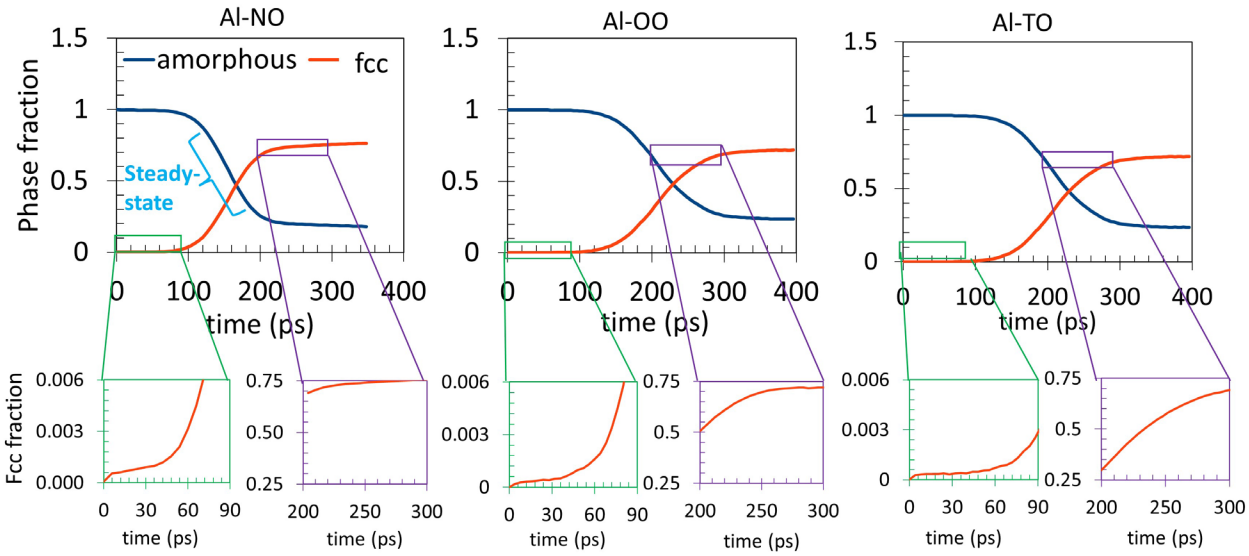

Figure 3. Time evolution of mean phase fraction (fcc and amorphous) during the solidification process for Al-NO, Al-OO, and AL-TO. Each data point for each time frame represents the mean phase fraction obtained from 400 bootstrap replications.

Results presented in Figure 2(b) and Figure 3 suggest that the oxides delay the overall solidification process and result in grain refinement in regions between the oxides. Therefore, as shown in Figure 5 (b), we analyzed the evolution of fcc phase fractions for regions A and B which represent regions in between and outside of the oxide clusters, respectively. Data presented in Figure 4(a) are based on the time evolution of mean fcc phase fraction based on 400 bootstrapping replicas in regions A and B. The python code for calculating results of Figure 4 (a) can be found in section 7 of the Supplementary Materials. The results clearly show that three oxides postpone the initiation of solidification in region A. In addition, the final fcc phase fraction after the completion of the solidification for Al-NO and Al-OO is almost similar. The difference between the fcc phase fractions in regions A and B for the AL-TO simulation is attributed to the higher numbers of GBs and TBs in region A compared to the region B. Earlier in this paper, we investigated the refined grain structures in between oxide layers. As discussed in the literature, the localized grain refinement affects the formation of TB structures. We will make further analysis on how the TB formation in regions A and B are affected by the oxides in section 3.3.

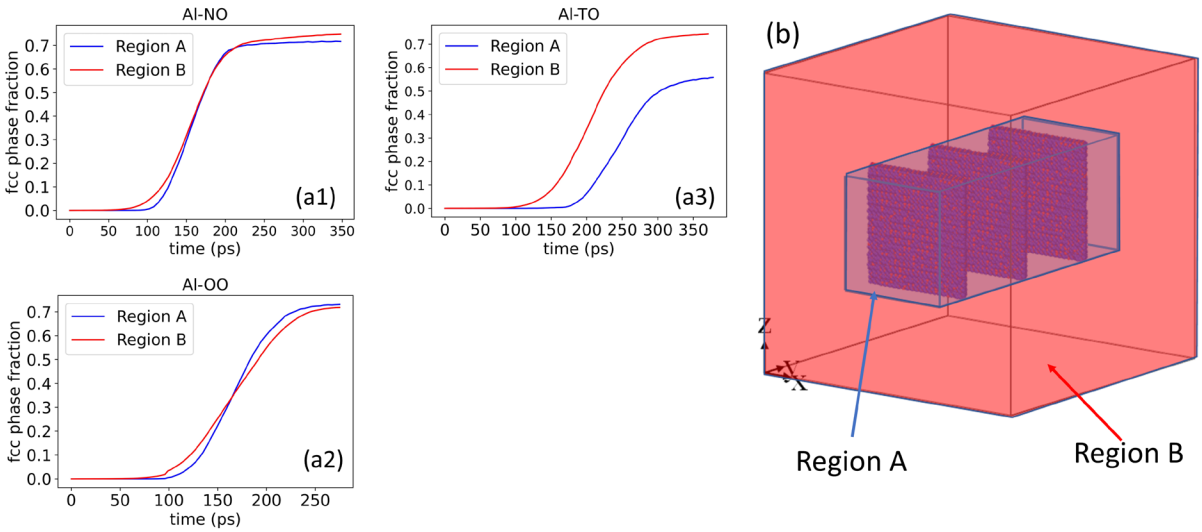

Figure 4. (a) Time evolution of mean fcc phase fraction during the solidification process for Al-NO, Al-OO, and AL-TO in regions A and B (b) Schematic presentation of Regions A and B. Each data point for each time frame represents the mean fcc phase fraction obtained from 400 bootstrap replications.

Having the largest solidification rate, one expects the orientation selection at the end of the Al-NO simulation to follow a more random distribution. A faster solidification velocity is equivalent to a more limited time for the atoms to select their orientations during the solidification process. This trend was observed in all three plots in Figure 5 (a), where the shape of angle distribution for Al-NO has a much wider distribution compared to the other two simulations. The shapes of the angle probability distributions for Al-OO and Al-TO are much closer to each other, and the three angles representing the peak values for Al-OO and Al-TO simulations are approximately (25, 35, 51) and (32, 38.5, 48), respectively.

To study how the delayed solidification alter the grain orientations, we calculated the probability distribution of orientation angles for regions A and B. Disregarding minor differences, all three cases present an almost identical angular distribution for the region B (outside of oxide cluster region) in comparison to the overall angular distribution (Figure 5 (a)). On the other hand, one can identify clear differences between the angular distributions for the region A of these three cases. A narrow distribution of angles in region B for Al-TO is observed because of the delayed solidification due to the presence of oxide layers followed by a rapid solidification once the phase transformation is initiated. All the results discussed here suggest

that although the oxide layers do not pose as favored nucleation sites, they clearly lead to heterogeneity in nanostructure and affect the orientation selection in regions close to the oxides.

Literature [76, 77] suggests the equilibrated Al-O bond length at the Al-Al_2O_3 interface is different from the bulk of the material. It is because the oxygen atoms diffuse to the surface of interface. As discussed by the experimental [76] and MD [77] studies, this phenomenon decreases the Al-Al_2O_3 interface energy and is responsible for the nonwetting to wetting transition of Al on Al_2O_3 as the temperature exceeds 1150 K. On the other hand, diffusion is a temperature-controlled process. As we undercool the simulation system well below the melting point, we limit the diffusion of oxygen atoms to the oxide surface. Therefore, we did not observe any heterogenous nucleation because the temperature was not high enough for the non-wetting to wetting transition. Our MD results in Figure 4 clearly show that Region A is the last region where solidification takes place for Al-TO system. Considering the large peak values in probability distributions in region A for Al-OO and AL-TO, there are certain grain orientations that are more favored in regions near the oxide surfaces, depending on the adhesion properties of solid Al-Al2O3 interfaces. Both experimental [74, 78] and numerical [71-73] studies suggest that, in addition to $(111)_{Al}||(0001)_{Al_2O_3}$, there are other preferred orientation relationships at the Al-Al_2O_3 interface such as $(\bar{1}10)_{Al}||(10\bar{1}0)_{Al_2O_3}$, $(\bar{1}2\bar{1})_{Al}||(10\bar{1}0)_{Al_2O_3}$, and $(5\bar{4}\bar{1})_{Al}||(10\bar{1}0)_{Al_2O_3}$.

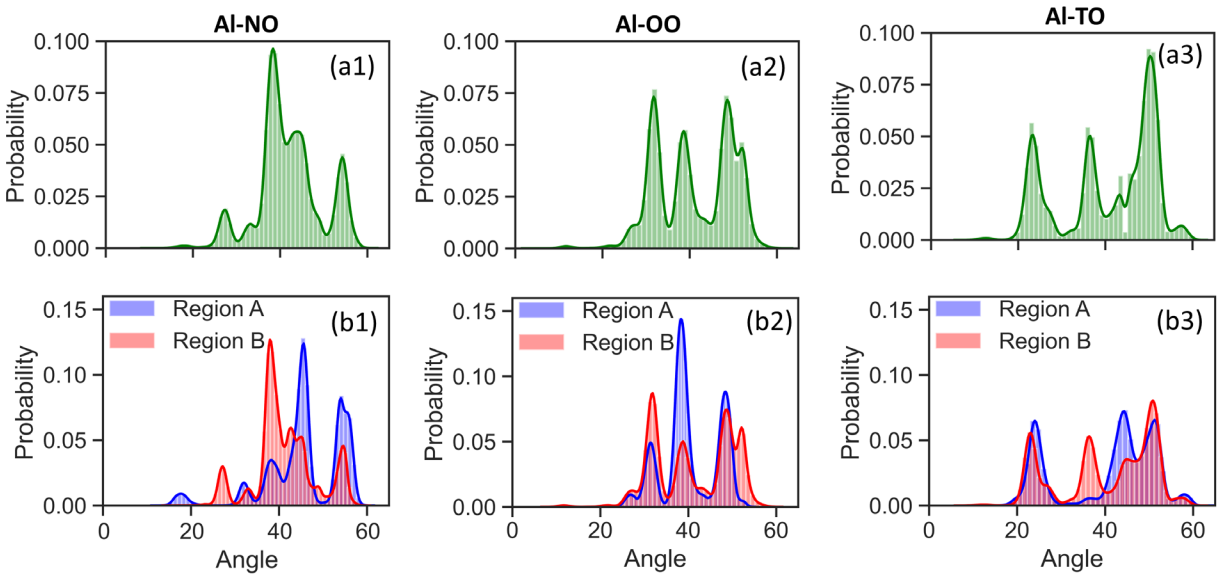

Figure 5. (a) Overall (left column) and (b) regional (right column) probability distributions of grain angle in the final nanostructure of Al-NO, AL-OO, and AL-TO.

3.2. Thermodynamic modeling of twin boundary formation on Al or Al_2O_3 substrate

During solidification, atoms inside the liquid phase locally attach to each other to form a solid nucleus. The initial nucleus may have a perfect fcc structure or contain some twins and/or stacking faults. In this section, we use thermodynamic modeling to explore the formation mechanism of perfect and twinned structures during the solidification of Al on Al or Al_2O_3 substrates. Figure 6 shows the schematic diagrams of three nuclei, one with a perfect fcc structure and the other two with lamellar and 5-fold twinned structures. Based on the terrace/ledge nucleation model [79], the total Gibbs free energy changes during the growth of a new cylinder-shaped layer with normal fcc stacking on the [111] plane on Al (ΔG_{Al}^{p}) and Al_2O_3 ($\Delta G_{Al_2O_3}^{p}$) substrates are given by [79]:

$$\Delta G_{Al}^{p} = [\pi r^2 h \Delta G_V] + 2\pi r h \gamma_{SL}, \quad (2)$$

$$\Delta G_{Al_2O_3}^{p} = \frac{1}{6}\pi\left[6r^2h + 3rh^2\left(\frac{2}{\tan\theta} - \frac{1+\cos\theta}{\sin\theta} - \frac{1+\cos\theta}{\sin\theta}\frac{1}{\tan\theta^2}\right) + h^3\left(1 + \frac{3}{\tan\theta^2}\right)\right]\Delta G_V + 2\pi r h \gamma_{SL}, \quad (3)$$

where γ_{SL} is the solid-liquid interface energy, r is the radius, h is the height of the new layer which is equal to the interatomic spacing in <111> direction, and θ is the wetting angle. The first terms inside the square brackets in Equations (2) and (3) denote the free energy change due to the phase transformation. ΔG_V is the bulk free energy per unit volume driving the nucleation process, given by $\Delta G_V = L(T - T_m)/T_m$, where L is the latent heat of fusion, T is the undercooled temperature, and T_m is the melting temperature. The last terms in Equations (2) and (3) are the energy contributions due to the formation of solid-liquid interface based on the terrace/ledge nucleation model.

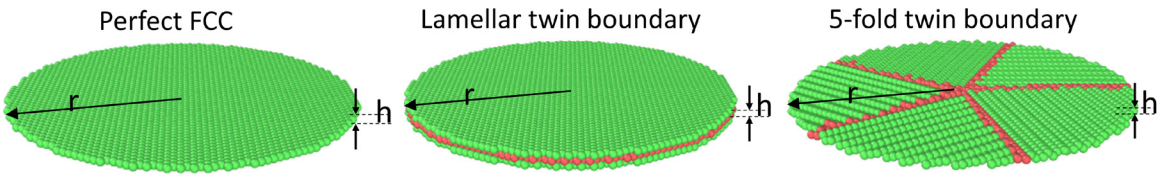

Figure 6. Schematic diagram of nucleation of a perfect fcc, lamellar and 5-fold TBs.

During solidification, the repeated nucleation of ledges on (111) terraces can follow a trend different than the ABCABC stacking of a perfect structure, such as ABCA**B**ACB. This represents a twinned sequence, and the bolded B represents the fault position. If the new layer is deposited with a twinned stacking, the total free energy change for lamellar (ΔG_{Al}^{Lam}, $\Delta G_{Al_2O_3}^{Lam}$) and 5-fold (ΔG_{Al}^{5F}, $\Delta G_{Al_2O_3}^{5F}$) on Al and Al_2O_3 substrates will include additional terms related the TB formation [79].

$$\Delta G_{Al}^{Lam} = \pi r^2 h \Delta G_V + 2\pi r h \gamma_{SL} + \pi r^2 \gamma_t \,, \tag{4}$$

$$\Delta G_{Al_2O_3}^{Lam} = \frac{1}{6}\pi\left[6r^2h + 3rh^2\left(\frac{2}{\tan\theta} - \frac{1+\cos\theta}{\sin\theta} - \frac{1+\cos\theta}{\sin\theta}\frac{1}{\tan\theta^2}\right) + h^3\left(1+\frac{3}{\tan\theta^2}\right)\right]\Delta G_V + 2\pi r h\gamma_{SL} + \pi r^2\gamma_t \,, \tag{5}$$

$$\Delta G_{Al}^{5F} = 2\pi r h \gamma_{SL} + \pi r^2 h \Delta G_V + 5\left(r + \frac{h}{2\times\tan\theta}\right)h\gamma_t \,, \tag{6}$$

$$\Delta G_{Al_2O_3}^{Lam} = \frac{1}{6}\pi\left[6r^2h + 3rh^2\left(\frac{2}{\tan\theta} - \frac{1+\cos\theta}{\sin\theta} - \frac{1+\cos\theta}{\sin\theta}\frac{1}{\tan\theta^2}\right) + h^3\left(1+\frac{3}{\tan\theta^2}\right)\right]\Delta G_V + 2\pi r h\gamma_{SL} + 5rh\gamma_t. \tag{7}$$

γ_t is the TB energy. Setting the derivatives of Equations (2-7) equal to zero, the critical nuclei size for the growth of perfect (r_c^P), lamellar (r_c^L), and 5-fold (r_c^{5F}) twinned structure on Al or Al_2O_3 substrates are given as:

$$r_c^p\big|_{Al} = -\frac{\gamma_{SL}}{\frac{L(T-T_m)}{T_m}}\,, \tag{8}$$

$$r_c^p\big|_{Al_2O_3} = -\frac{\gamma_{SL}}{\frac{L(T-T_m)}{T_m}} - \frac{h}{4}\left(\frac{2}{\tan\theta} - \frac{1+\cos\theta}{\sin\theta} - \frac{1+\cos\theta}{\sin\theta}\frac{1}{\tan\theta^2}\right), \tag{9}$$

$$r_c^{Lam}\big|_{Al} = -\frac{\gamma_{SL}}{\frac{L(T-T_m)}{T_m} + \frac{\gamma_t}{h}}\,, \tag{10}$$

$$r_c^{Lam}|_{Al_2O_3} = -\frac{\gamma_{SL}+\frac{h}{4}\left(\frac{2}{\tan\theta}-\frac{1+\cos\theta}{\sin\theta}-\frac{1+\cos\theta}{\sin\theta}\frac{1}{\tan\theta^2}\right)\times\frac{L(T-T_m)}{T_m}}{\frac{L(T-T_m)}{T_m}+\frac{\gamma_t}{h}}, \quad (11)$$

$$r_c^{5F}|_{Al} = -\frac{\gamma_{SL}+\frac{5}{2\pi}\gamma_t}{\frac{L(T-T_m)}{T_m}}, \quad (12)$$

$$r_c^{5F}|_{Al_2O_3} = -\frac{\gamma_{SL}+\frac{h}{4}\left(\frac{2}{\tan\theta}-\frac{1+\cos\theta}{\sin\theta}-\frac{1+\cos\theta}{\sin\theta}\frac{1}{\tan\theta^2}\right)\times\frac{L(T-T_m)}{T_m}+\frac{5}{2\pi}\gamma_t}{\frac{L(T-T_m)}{T_m}}. \quad (13)$$

The Gibbs free energies and critical radiuses for the growth of perfect and lamellar TB or 5-fold TB structures on the Al substrate can be obtained by setting the wetting angles in the corresponding equations for the growth on Al_2O_3 substrate to θ=90°.

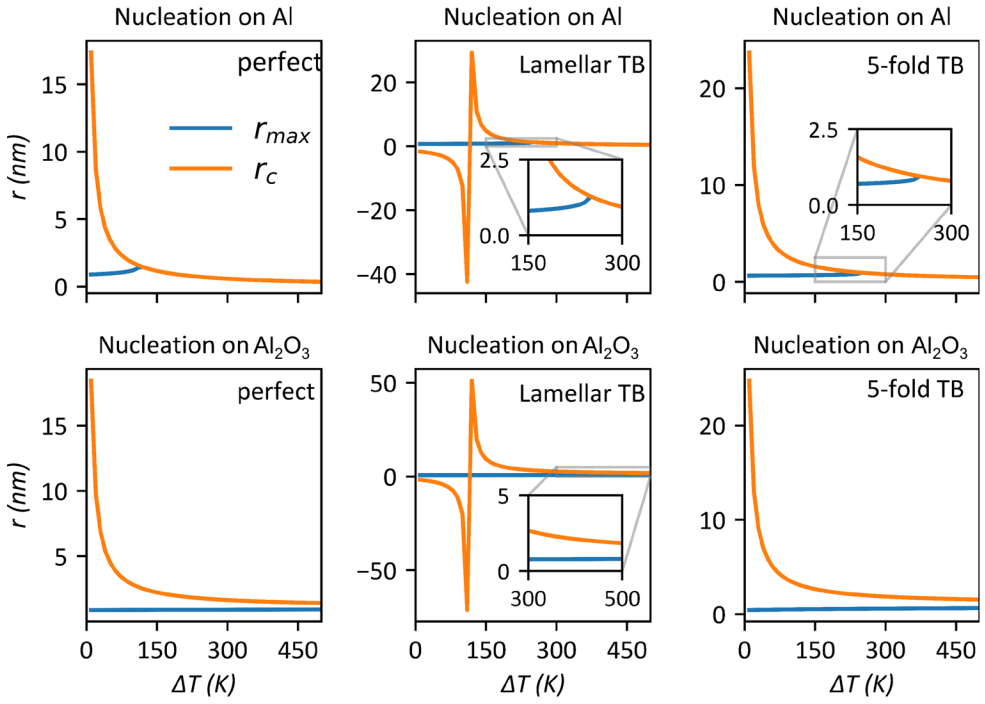

Figure 7. Critical radius (r_c) and maximum radius of nuclei (r_{max}) verus undecooling during the growth of perfect, lamellar twinned, and 5-fold twinned structures on Al and Al_2O_3 substrates.

For r smaller than the critical nucleus size, the system lowers its free energy by dissolution of the solid/nucleus. As r surpasses the critical value, the free energy of the system decreases as the system solidifies and the nucleus gets larger. All the details of thermodynamic

modeling are incorporated into a python code, and one can plug in the required material properties to investigate the growth of perfect or twinned structures. In this study, the bulk solid-liquid and TB energies for Al are estimated as $\gamma_{SL} = 0.177$ J/m^2 [80] and $\gamma_t = 0.08$ J/m^2 [81], respectively. Various investigations [82-86] of the wettability of Al on a Al_2O_3 substrate showed that the wettability drops below 90° as the temperature exceeds the melting point of Al. However, undercooling increases the wetting angle, and θ≈157° when the melt temperature drops to 500 K [82]. Figure 7 summarizes the evolution of critical nucleus size with undercooling during the growth of perfect, lamellar TB, and 5-fold TB structures on Al or Al_2O_3 substrates. For the growth of perfect and 5-fold twinned structures on both Al and Al_2O_3 substrates, as undercooling increases, the critical nuclei size decreases. However, the evolution of critical nucleus size with undercooling during the growth of lamellar TB is more complicated (given by Equations (10) and (11)). The graphical visualization of the critical radius for the growth of lamellar TB suggests that its growth on Al and Al_2O_3 substrates is impossible unless the undercooling exceeds ~115 K. This is attributed to the non-physical negative critical radius when the undercooling is below the given threshold. The threshold for the lamellar TB growth (t^{Lam}) on both Al and Al_2O_3 substrates can also be estimated by:

$$t^{Lam}|_{Al} = t^{Lam}|_{Al_2O_3} = T_m\,\gamma_t/Lh. \qquad (14)$$

For an undercooling smaller than 115 K, $r_c^L < 0$, and consequently it is impossible to nucleate lamellar TBs. However, undercoolings larger than the aforementioned threshold does not guarantee the formation of "stable" nuclei. Undercooling larger than 115 K is necessary but insufficient to promote the formation of lamellar twinned structure.

Inside the liquid phase, numerous closed-packed crystal-like clusters of various sizes are present. As the size of the cluster reaches the critical value, it forms a stable solid nucleus. The number of spherical clusters of radius r (n_r) is given by [87]:

$$n_r = n_0 exp\left(-\frac{\Delta G_r}{k_B T}\right), \qquad (15)$$

where n_0 is the total number of atoms in the system, ΔG_r is the excess free energy associated with the cluster, and k_B is the Boltzman constant. For each undercooled temperature, n_r decreases exponentially with increase of ΔG_r, suggesting lower probability of finding larger clusters inside the liquid phase. Our MD simulations include approximately 1.6 M atoms, and we

estimated nucleation rate to be 2.35×10^{35} $m^{-3}s^{-1}$ during ~300 ps of solidification. Plugging in the aforementioned data into Equation (15) gives the available free energy $\sim 52\, k_B T$. Using Equations (2-7) and (15), the maximum size of the cluster that has a reasonable probability of occurrence in the liquid phase, r_{max}, can be calculated for the growth of perfect and twinned structures at various temperatures. Details on calculations of maximum radius are also included in the python code which can be found in section 6 of the Supplementary Materials. In addition to the critical nucleus size, Figure 7 presents the variations of maximum cluster size versus undercooling temperatures. During solidification of a perfect fcc structures on Al and Al_2O_3 substrates, r_c is much larger than r_{max} when the undercooling is small. This means the odds of forming a stable nucleus on the surface of Al substrate for small undercooling are very low. As the undercooling exceeds ~110 K, the critical nuclei size drops below the maximum cluster radius meaning that there is a good chance for the cluster to turn into a stable nucleus when perfect structure grows on Al substrate. However, the formation of perfect structure on Al_2O_3 substrate is not possible even for undercooling as large as 440 K. Therefore, the odds for formation of perfect structures on Al_2O_3 substrate are very low.

The variations of r_c and r_{max} with undercooling during the growth of 5-fold TBs are qualitatively similar to the graphs of perfect structure. When the undercooling is small, r_{max} profile lies below r_c. Growth of stable 5-fold TB on Al substrate takes place when the undercooling exceeds 245 K. However, during the growth of 5-fold TB on Al_2O_3 substrate, r_{max} is always smaller than r_c for undercoolings up to 440 K. Therefore, it is energetically impossible to form a 5-fold TB on the Al_2O_3 substrate.

For undercoolings below 115 K, critical nucleus size for lamellar TB has a negative value which does not have a physical meaning. However, undercooling larger than this threshold does not guarantee the formation of stable nuclei out of all the clusters inside the melt. Based on the critical and maximum radius variations versus undercooling, the critical undercooling required for the formation of a stable nucleus with a lamellar twinned structure on the Al substrate is ~245 K. Therefore, homogenous nucleation of a lamellar twinned structure occurs when the liquid undercooling is ~245 K. It should be mentioned that the formation of clusters larger than r_{max} is possible, but the probability of finding them is very small as they either melt or turn into a stable nucleus. On the other hand, the formation of a lamellar twinned structure on the Al_2O_3 substrate

is energetically impossible because the maximum radius figure always lies below the critical nucleus size.

Overall, comparing the critical nuclei radius for the six cases presented in Figure 7 suggests that in the range of investigated undercooling (up to 500 K), the odds of formation of perfect and twinned structures on an Al_2O_3 substrate is very low. On the other hand, the formation of prefect/lamellar and 5-fold twinned structures on the Al substrate is energetically favorable. However, the nucleation of a perfect crystal on Al substrate is always preferred to a twinned one. This is because the minimum required undercooling is smaller and the maximum cluster size is larger for the growth of a perfect structure compared with those of the twinned structures. This difference drops when the solidification driving force (undercooling) increases or the material has smaller TB energies. In addition, the undercooling threshold required for the formation of both lamellar and 5-fold twinned structures is around 245 K. This suggests that they have a similar change to nucleate on an Al substrate.

The change in free energy versus the nucleus size for ΔT=140 K and 440 K is presented in Figure 8. As suggested previously, 140 K undercooling only provides sufficient driving force to form a stable, perfect-structured nucleus. At ΔT=140 K, the free energy required to form a critical nucleus size with twinned structures (both lamellar and 5-fold) is larger than $52\ k_BT$ which is the free energy available during our MD simulations. Thus, perfect structures can be formed from a 140 K undercooled melt Al on the Al substrate but the probability of nucleation of a twinned structure is zero. From Figure 7, ΔT=110, 245, and 245K are the minimum undercooling needed to form perfect fcc, 5-fold TB, and lamellar TB, respectively. As the ΔT drops to 245 K, below the aforementioned critical thresholds, the formation of both fcc and TBs is possible. However, the perfect structure is still energetically more favored and the majority of atoms in the solidified system follow the fcc stacking order.

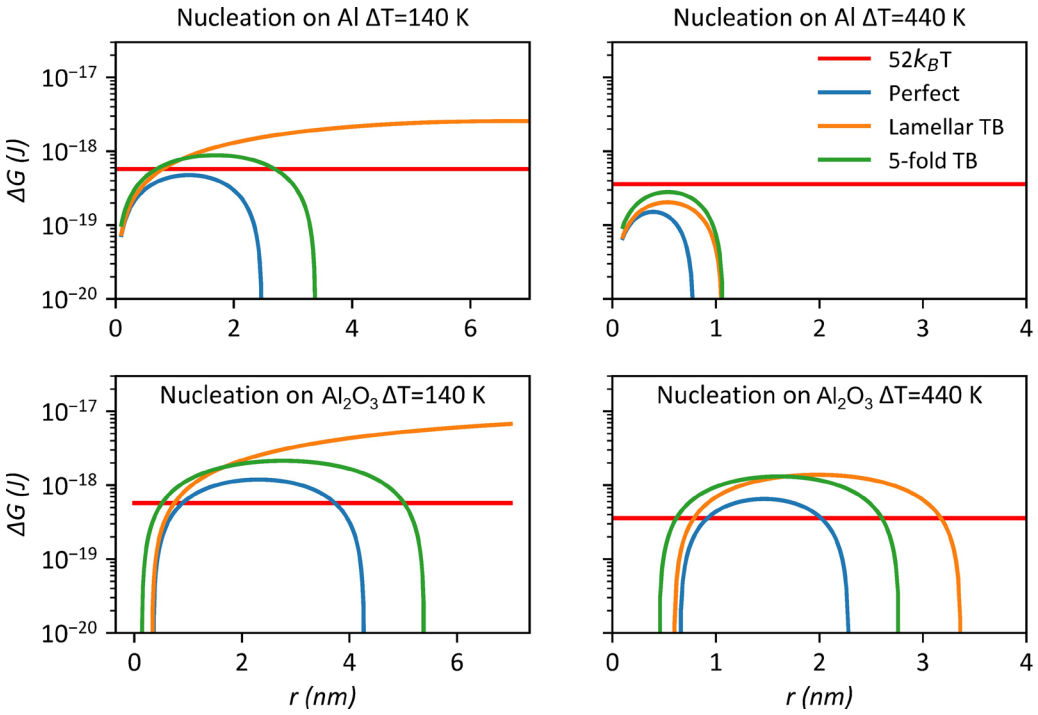

Figure 8. Change in free energy with the cluster size during the solidification of perfect fcc structure, lamellar TB, and 5-fold TB under undercooling of 140 K and 440 K.

3.3. Growth of 5-fold and lamellar twin boundaries

The results presented is Figure 2 clearly show refined grains in regions between the oxide layers. Analyzing the evolution of the nanostructure reveals that having oxides in the simulation system delays the solidification process and the regions near the oxide solidify last. Therefore, the temperature in these regions may locally drop while the solidification still has not taken place [23-25]. This promotes the formation of smaller grains as soon as solidification starts, which was discussed in Figure 2 (b). On the other hand, the results in Figure 9(a) clearly demonstrate that the regions which solidified last tends to form larger amounts of defects. The simulation system crystallized from melt possesses a high concentration of defects (stacking faults, TBs, voids) due to the natural process of crystallization which are all embedded inside the FCC matrix. Previous studies reported excess fractions of TBs observed during solidification of Al-Zn [29, 30], pure Al [31] and Au–Cu–Ag [30] with small alloying elements of Cr, Ti, and Ir, respectively. Also, the formation of icosahedral short-range order in undercooled liquid leads to the growth of iQC. The coherent orientation relationships (ORs) developed between iOC particles and the fcc grains lead

to the formation of TBs [30]. But these studies could not explain the large increase of TBs accompanied by grain refinement. In addition, iQc are identified as building blocks for fivefold symmetry, leading to the formation of 5-fold twin grains. Our simulations suggest that lamellar twined structures are also formed in the grain refined regions.

Figure 5 suggests that the oxide clusters affect the grain orientations in between oxide layers. The narrow distributions of both grain angles and TB fraction in regions A for Al-OO and Al-TO support the hypothesis that the refined grains are prone to form twinned structures. The simulation temperature is way below the nonwetting-wetting transition temperature of 1150 K, which slows down the diffusion of oxygen to the Al-Al_2O_3 interface. Therefore, the oxygen concentration at the interface is not large enough to modify the bonding between Al-O. However, it is high enough to affect the orientations of iQC formed in between oxide layers, and we attribute the narrow distribution of grain orientations to the bond formed between Al-O at the Al-Al_2O_3 interface.

In our analysis, the nanostructure of the case with no oxides tends to have an almost homogenous distribution of TBs and grains in the system. The heterogeneity in the nanostructure of the cases with one and three oxide clusters resonances in the variations of number of grains and volume fraction of TBs in the simulation system. This is much clearer for Al-TO, where the small grains tend to have a larger ratio of growth TBs to the volume of grain. The refined microstructure and high density of TBs affect the deformation mechanism, as the separation between twins must exceed a certain value as the dislocation tries to propagate through the TB [88]. We attribute the origin of the high TB fraction to the preferred orientation relationships at the solid Al-Al_2O_3 interface [71-74, 78].

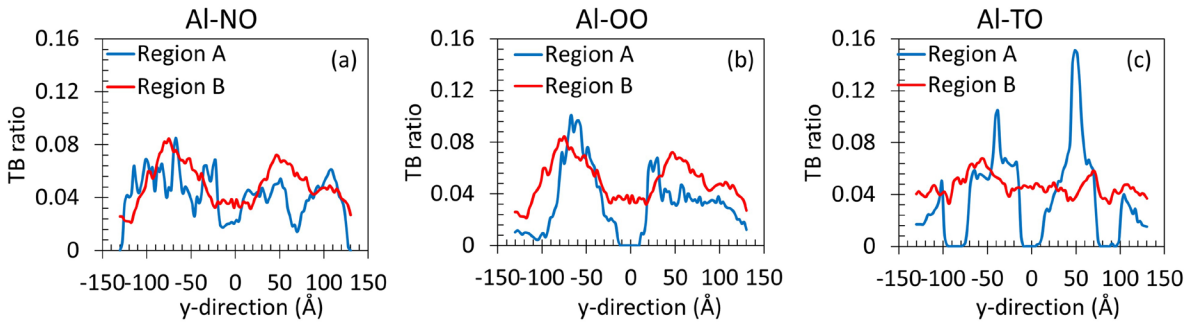

Figure 9. The regional variations of TBs ratio (given by the ratio of number of atoms with TB structure to the total number of atoms in the sub-divisions) in the solidified nanostructure along the y-direction for (a) Al-NO, (b) Al-OO, and (c) Al-TO simulations.

Following the thermodynamic modeling of the growth twin formation, we conducted further investigations to unravel the mechanisms governing the formation of various TBs. The formation of 5-fold annealing and deformation twins has been reported by both experimental [89-92] and MD [93, 94] studies. Song et al. recently reported 5-fold TB formation mechanisms through embedding nano particles in an organic matrix on a transmission electron microscope grid and studied the oriented attachment [95]. This promising work was the first experimental evidence of 5-fold TBs growth via both the layer-by-layer addition and decomposition of high-energy grain boundaries in both low (Au) and high (Pt) stacking fault energy materials. However, the same mechanism was not presented for the solidification studies. We present the first computational evidence supporting the formation of 5-fold twins during solidification based on both mechanisms in Figure 10. The layer-by-layer addition of twinned boundaries starts at t=110 ps (shown by the black circle) and the layer-wise addition of fcc with 5-fold twin continues until t=200 ps. The second mechanism is shown by the blue circle, where the grain boundary between two adjacent grains decomposes starting from t=150 ps and continuing up to t=400 ps, where the full 5-fold twinned structure is decomposed from the grain boundary.

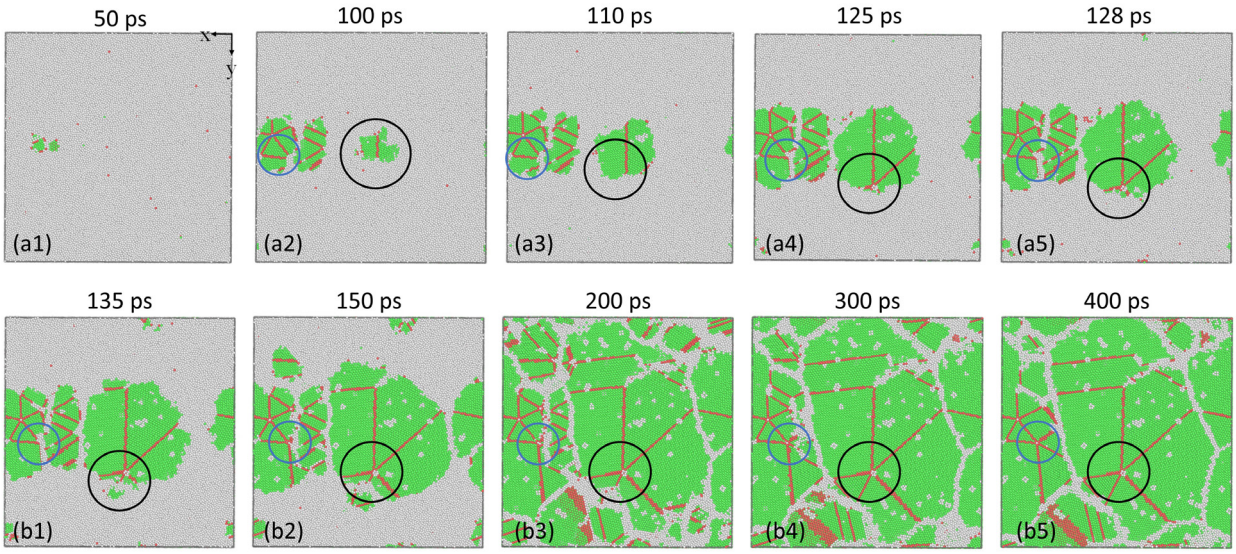

Figure 10. Snapshots from the MD simulation of Al-TO presenting the two mechanisms governing the formation of 5-fold twins during the solidification.

Conclusion

It is very challenging, if not impossible, for the current experimental techniques to monitor the nano- and micro-structural evolutions during the transient and highly localized phenomena associated with the solidification process. The presence of oxides during solidification is often unavoidable, and it affects the micro/nanostructure evolution (grain size, orientation, defects) and nucleation process. In this research, we performed several MD simulations to investigate how Al_2O_3 clusters inside the aluminum melt affect the grain structure formation, grain orientation selection, and defect formation and evolution during solidification. For the first time, in this study, we applied the matrix representation method as a tool for analyzing the nucleation process inside the melt. This helped us to 1) have a better presentation of the structural evolution during the solidification, 2) accurately visualize the individual grains and characterize TBs, and 3) trace uncommon phenomena during solidification, such as the importance of grain orientation during the Oswald Ripening process, which was not observed previously.

The main findings of this work can be summarized as:

- The presence of oxide layers in the melt results in inhomogeneity of grain size distribution, which affects the characteristic orientation selections and distribution of defects inside the solidified nanostructure. Oxide surfaces do not serve as heterogenous nucleation sites for solidification. However, the refined structures in their vicinity lead to heterogeneity in the final nanostructure.
- The overall solidification time for the case with no oxides was shorter than other cases. For the case with three oxide layers, the delayed nucleation and delayed steady-state stage of solidification (the region with almost linear time evolution of amorphous phase fraction) resulted in localized refinement of grains near the oxide clusters. The solidification delay mostly took place in areas between oxide layers.
- Oxides alter the nanostructures by refining grains in regions between the oxide clusters, increasing the number of twinned grains, and changing the distribution of grain orientation selection. Based on our analysis, the nanostructure heterogeneity is caused by a number of factors, including 1) nonwetting properties of the liquid Al-Al_2O_3 interface, 2) delayed nucleation at regions near the oxide layers, 3) insufficient temperature for diffusion of oxygen atoms to the Al_2O_3 surface, and 4) orientation relationships at the solid Al-Al_2O_3 interface.
- The thermodynamic modeling based on the terrace-ledge method enabled us to identify the possibility of perfect fcc, lamellar twin, and 5-fold twin formation during the solidification of aluminum on Al and Al_2O_3 substrates. The critical nucleus radius for the formation of stable fcc and twinned 5-fold structures follow a descending behavior with temperature. On the other hand, the critical radius variations with undercooling during the growth of lamellar twinned structures exhibit a hyperbolic shape. This makes it thermodynamically impossible to form lamellar twinned structure below an undercooling threshold. This undercooling threshold depends on the TB energy, the melting temperature, enthalpy of fusion and the interatomic spacing in aluminum. However, undercoolings larger than this threshold does not guarantee the formation of lamellar twinned structures.

  An accurate prediction of critical undercooling for each manufacturing technique or simulation method depends on the intersect of critical radius and maximum cluster size variations with undercooling. Investigation on the variations of critical and maximum

radius, for undercoolings up to 500 K, suggests the odds of formation of perfect and twinned structures (both lamellar and 5-fold) on an Al_2O_3 substrate is almost zero. The critical undercooling temperatures for the growth of fcc, 5-fold, and lamellar structures on Al substrate are 110, 245, and 245 K, respectively.

- Finally, we provided the first computational proof of 5-fold TB formation during solidification indicating that in addition to previously shown layer-by-layer addition, grain boundary deposition is another mechanism governing the formation of 5-fold TBs during the solidification process, similar to Song et al. experiments [95].

Acknowledgment
This study was supported by the National Science Foundation, CMMI 2031800. We are grateful for the supercomputing time allocation provided by the NSF's ACCESS (Advanced Cyberinfrastructure Coordination Ecosystem: Services & Support), Award No. TG-DMR140008.

CRediT Author Statement
Sepideh Kavousi: Conceptualization, Methodology, Software, Formal analysis, Writing-Original Draft Preparation. **Mohsen Asle Zaeem:** Supervision, Conceptualization, Methodology, Formal analysis, Writing- Reviewing and Editing, Funding Acquisition.

Data availability
All the necessary data generated or analyzed in this study and the associated Python codes are included in this published article and its Supplementary Materials; other auxiliary data are available from the corresponding author on reasonable request.

Declaration of Competing Interest
The authors declare no competing interests.

References:

[1] J. Campbell, „Bifilms–The Most Exciting Discovery Of The Century ", Shape Casting: John Campbell Symposium, TMS, 2005.
[2] J. Campbell, Metallurgy without Bifilms: No More Fractures, Shape Casting: 5th International Symposium 2014, Springer, 2014, pp. 163-170.
[3] J. Campbell, Complete casting handbook: metal casting processes, metallurgy, techniques and design, Butterworth-Heinemann2015.

[4] D. Dispinar, J. Campbell, Use of bifilm index as an assessment of liquid metal quality, International Journal of Cast Metals Research 19(1) (2006) 5-17.
[5] D. Dispinar, C. Kahruman, J. Campbell, Correlation between Bifilm Index and Toughness of Aluminum Alloys, Shape Casting: 5th International Symposium 2014, Springer, 2014, pp. 171-176.
[6] M. Tiryakioğlu, J. Campbell, C. Nyahumwa, Fracture surface facets and fatigue life potential of castings, Metallurgical and Materials Transactions B 42(6) (2011) 1098-1103.
[7] G.E. Fuchs, M.A. Kaplan, Investigation of Oxide Bifilms in Investment Cast Superalloy IN100: Part I. Mechanical Properties, Metallurgical and Materials Transactions A 47(5) (2016) 2346-2361.
[8] D.Z. Li, J. Campbell, Y.Y. Li, Filling system for investment cast Ni-base turbine blades, Journal of Materials Processing Technology 148(3) (2004) 310-316.
[9] J. Campbell, Entrainment defects, Materials Science and Technology 22(2) (2006) 127-145.
[10] J. Campbell, An overview of the effects of bifilms on the structure and properties of cast alloys, Metallurgical and Materials Transactions B 37(6) (2006) 857-863.
[11] T. Tunçay, S. Tekeli, D. Özyürek, D. Dişpinar, Microstructure–bifilm interaction and its relation with mechanical properties in A356, International Journal of Cast Metals Research 30(1) (2017) 20-29.
[12] H. Bagherpour-Torghabeh, R. Raiszadeh, H. Doostmohammadi, Role of Mechanical Stirring of Al-Mg Melt in the Healing of Bifilm Defect, Metallurgical and Materials Transactions B 48(6) (2017) 3174-3184.
[13] M. El-Sayed, H. Hassanin, K. Essa, Bifilm defects and porosity in Al cast alloys, The International Journal of Advanced Manufacturing Technology 86(5-8) (2016) 1173-1179.
[14] A. Halvaee, J. Campbell, Critical mold entry velocity for aluminum bronze castings, One Hundred First Annual Meeting of the American Foundrymen's Society, Rosemont, 1997, pp. 35-46.
[15] M. Cross, D. McBride, T. Croft, A. Williams, K. Pericleous, J. Lawrence, Computational modeling of mold filling and related free-surface flows in shape casting: An overview of the challenges involved, Metallurgical and Materials Transactions B 37(6) (2006) 879-885.
[16] J. Campbell, Quality Castings: A Personal History of the Development of the Cosworth Casting Process, Aspect Design, Malvern (2014).
[17] P. Samimi, Y. Liu, I. Ghamarian, P.C. Collins, A novel tool to assess the influence of alloy composition on the oxidation behavior and concurrent oxygen-induced phase transformations for binary Ti–xMo alloys at 650°C, Corrosion Science 89 (2014) 295-306.
[18] M. Emamy, B. Pourbahari, M. Malekan, K. Emami, Effects of Mg 2 Sn intermetallic on the microstructure and tensile properties of Al–15% Mg 2 Si–X% Sn composite, Journal of Materials Research 31(24) (2016) 3891-3899.
[19] J. Campbell, Chapter 2 - Entrainment, in: J. Campbell (Ed.), Complete Casting Handbook (Second Edition), Butterworth-Heinemann, Boston, 2015, pp. 17-90.
[20] J. Campbell, The origin of Griffith cracks, Metallurgical and Materials Transactions B 42(6) (2011) 1091-1097.
[21] W. Khalifa, F.H. Samuel, J.E. Gruzleski, Nucleation of solid aluminum on inclusion particles injected into Al-Si-Fe alloys, Metallurgical and Materials Transactions A 35(10) (2004) 3233-3250.
[22] H.T. Li, Y. Wang, Z. Fan, Mechanisms of enhanced heterogeneous nucleation during solidification in binary Al–Mg alloys, Acta Materialia 60(4) (2012) 1528-1537.
[23] T. Atamanenko, D. Eskin, L. Zhang, L. Katgerman, Criteria of grain refinement induced by ultrasonic melt treatment of aluminum alloys containing Zr and Ti, Metallurgical and Materials Transactions A 41(8) (2010) 2056-2066.
[24] G.I. Eskin, Broad prospects for commercial application of the ultrasonic (cavitation) melt treatment of light alloys, Ultrasonics Sonochemistry 8(3) (2001) 319-325.
[25] N. Balasubramani, D. StJohn, M. Dargusch, G. Wang, Ultrasonic Processing for Structure Refinement: An Overview of Mechanisms and Application of the Interdependence Theory, Materials (Basel) 12(19) (2019) 3187.

[26] J. Walker, Physical chemistry of process metallurgy, Part 2 (1961) 845-53.
[27] C. Puncreobutr, A.B. Phillion, J.L. Fife, P. Rockett, A.P. Horsfield, P.D. Lee, In situ quantification of the nucleation and growth of Fe-rich intermetallics during Al alloy solidification, Acta Materialia 79 (2014) 292-303.
[28] X. Cao, J. Campbell, The nucleation of Fe-Rich phases on oxide films in Al-11.5Si-0.4Mg cast alloys, Metallurgical and Materials Transactions A 34(7) (2003) 1409-1420.
[29] G. Kurtuldu, P. Jarry, M. Rappaz, Influence of Cr on the nucleation of primary Al and formation of twinned dendrites in Al–Zn–Cr alloys: Can icosahedral solid clusters play a role?, Acta Materialia 61(19) (2013) 7098-7108.
[30] M. Rappaz, G. Kurtuldu, Thermodynamic Aspects of Homogeneous Nucleation Enhanced by Icosahedral Short Range Order in Liquid Fcc-Type Alloys, JOM 67(8) (2015) 1812-1820.
[31] Z. Chen, J. Gao, K. Yan, Formation of twin boundaries in commercial purity aluminum with addition of Ti refiner, Materials Letters 221 (2018) 1-3.
[32] L. Lu, Y. Shen, X. Chen, L. Qian, K. Lu, Ultrahigh Strength and High Electrical Conductivity in Copper, Science 304(5669) (2004) 422-426.
[33] L.E. Murr, Interfacial phenomena in metals and alloys, (1975).
[34] Y. Shen, L. Qian, X. Chen, K. Lu, L. Lu, Science--Ultrahigh Strength and High Conductivity in Cu--Science, 2013.
[35] X. Zhang, O. Anderoglu, R.G. Hoagland, A. Misra, Nanoscale growth twins in sputtered metal films, JOM 60(9) (2008) 75-78.
[36] D. Bufford, Y. Liu, Y. Zhu, Z. Bi, Q.X. Jia, H. Wang, X. Zhang, Formation Mechanisms of High-density Growth Twins in Aluminum with High Stacking-Fault Energy, Materials Research Letters 1(1) (2013) 51-60.
[37] K.Y. Yu, D. Bufford, Y. Chen, Y. Liu, H. Wang, X. Zhang, Basic criteria for formation of growth twins in high stacking fault energy metals, Applied Physics Letters 103(18) (2013) 181903.
[38] A. Mahata, M. Asle Zaeem, Evolution of solidification defects in deformation of nano-polycrystalline aluminum, Computational Materials Science 163 (2019) 176-185.
[39] A. Mahata, M. Asle Zaeem, M.I. Baskes, Understanding homogeneous nucleation in solidification of aluminum by molecular dynamics simulations, Modelling and Simulation in Materials Science and Engineering 26(2) (2018) 025007.
[40] A. Mahata, T. Mukhopadhyay, M. Asle Zaeem, Liquid ordering induced heterogeneities in homogeneous nucleation during solidification of pure metals, Journal of Materials Science & Technology 106 (2022) 77-89.
[41] A.J. Shahani, P.W. Voorhees, Twin-mediated crystal growth, Journal of Materials Research 31(19) (2016) 2936-2947.
[42] I.J. Beyerlein, X. Zhang, A. Misra, Growth Twins and Deformation Twins in Metals, Annual Review of Materials Research 44(1) (2014) 329-363.
[43] Z. Zhang, S. Huang, L. Chen, Z. Zhu, D. Guo, Formation mechanism of fivefold deformation twins in a face-centered cubic alloy, Scientific Reports 7(1) (2017) 45405.
[44] T. Al, H. Rollnik, N. Al, V. Yamakov, D. Wolf, S. Phillpot, H. Gleiter, F. Karlsruhe, Dislocation Processes and Deformation Twinning in Nanocrystalline Al, 2002 International Conference on Computational Nanoscience and Nanotechnology - ICCN 2002 (2002).
[45] A. Mahata, T. Mukhopadhyay, M. Asle Zaeem, Modified embedded-atom method interatomic potentials for Al-Cu, Al-Fe and Al-Ni binary alloys: From room temperature to melting point, Computational Materials Science 201 (2022) 110902.
[46] J. Felsenstein, CONFIDENCE LIMITS ON PHYLOGENIES: AN APPROACH USING THE BOOTSTRAP, Evolution 39(4) (1985) 783-791.

[47] B. Efron, Bootstrap Methods: Another Look at the Jackknife, The Annals of Statistics 7(1) (1979) 1-26, 26.
[48] A.P. Thompson, H.M. Aktulga, R. Berger, D.S. Bolintineanu, W.M. Brown, P.S. Crozier, P.J. in 't Veld, A. Kohlmeyer, S.G. Moore, T.D. Nguyen, R. Shan, M.J. Stevens, J. Tranchida, C. Trott, S.J. Plimpton, LAMMPS - a flexible simulation tool for particle-based materials modeling at the atomic, meso, and continuum scales, Computer Physics Communications 271 (2022) 108171.
[49] A. Stukowski, Visualization and analysis of atomistic simulation data with OVITO–the Open Visualization Tool, Modelling and Simulation in Materials Science and Engineering 18(1) (2009) 015012.
[50] Y. Shibuta, S. Sakane, E. Miyoshi, S. Okita, T. Takaki, M. Ohno, Heterogeneity in homogeneous nucleation from billion-atom molecular dynamics simulation of solidification of pure metal, Nature Communications 8(1) (2017) 10.
[51] S. Ratanaphan, Y. Yoon, G.S. Rohrer, The five parameter grain boundary character distribution of polycrystalline silicon, Journal of Materials Science 49(14) (2014) 4938-4945.
[52] J.W. Jhang, T. Jain, H.K. Lin, C.W. Lan, Possible Twinning Operations during Directional Solidification of Multicrystalline Silicon, Crystal Growth & Design 18(4) (2018) 2518-2524.
[53] P.M. Larsen, S. Schmidt, J. Schiøtz, Robust structural identification via polyhedral template matching, Modelling and Simulation in Materials Science and Engineering 24(5) (2016) 055007.
[54] J.A. Dantzig, M. Rappaz, Solidification: -Revised & Expanded, EPFL press2016.
[55] J. Bragard, A. Karma, Y.H. Lee, M. Plapp, Linking Phase-Field and Atomistic Simulations to Model Dendritic Solidification in Highly Undercooled Melts, Interface Science 10(2) (2002) 121-136.
[56] J.J. Hoyt, M. Asta, A. Karma, Method for Computing the Anisotropy of the Solid-Liquid Interfacial Free Energy, Physical Review Letters 86(24) (2001) 5530-5533.
[57] J. Hoyt, M. Asta, A. Karma, Method for computing the anisotropy of the solid-liquid interfacial free energy, Physical review letters 86(24) (2001) 5530.
[58] J.J. Hoyt, M. Asta, Atomistic computation of liquid diffusivity, solid-liquid interfacial free energy, and kinetic coefficient in Au and Ag, Physical Review B 65(21) (2002) 214106.
[59] L. Boltzmann, Ein Wort der Mathematik an die Energetik, Annalen der Physik 293(1) (1896) 39-71.
[60] W. Ostwald, Über die vermeintliche Isomerie des roten und gelben Quecksilberoxyds und die Oberflächenspannung fester Körper, Zeitschrift für Physikalische Chemie 34U(1) (1900) 495-503.
[61] A. Kneissl, H. Fischmeister, Solidification and Ostwald Ripening of Near-Monotectic Zinc-Lead Alloys, Science 225(4658) (1984) 198-200.
[62] M. Suzuki, R. Yamaguchi, K. Murakami, M. Nakada, Inclusion Particle Growth during Solidification of Stainless Steel, ISIJ International 41(3) (2001) 247-256.
[63] A.J. Shahani, X. Xiao, K. Skinner, M. Peters, P.W. Voorhees, Ostwald ripening of faceted Si particles in an Al-Si-Cu melt, Materials Science and Engineering: A 673 (2016) 307-320.
[64] V. Turlo, O. Politano, F. Baras, Microstructure evolution and self-propagating reactions in Ni-Al nanofoils: An atomic-scale description, Journal of Alloys and Compounds 708 (2017) 989-998.
[65] N.J. Whisler, T.Z. Kattamis, Ostwald ripening during solidification of nondendritic spherical structures, Journal of Materials Science 7(8) (1972) 888-894.
[66] S.A. Kukushkin, Theory of the Ostwald ripening of new-phase nuclei in single-component melts, Acta Metallurgica et Materialia 43(2) (1995) 715-722.
[67] S. Kavousi, A. Gates, L. Jin, M. Asle Zaeem, A temperature-dependent atomistic-informed phase-field model to study dendritic growth, Journal of Crystal Growth 579 (2022) 126461.
[68] S. Kavousi, B.R. Novak, M.I. Baskes, M. Asle Zaeem, D. Moldovan, Modified embedded-atom method potential for high-temperature crystal-melt properties of Ti–Ni alloys and its application to phase field simulation of solidification, Modelling and Simulation in Materials Science and Engineering 28(1) (2019) 015006.

[69] S. Kavousi, B.R. Novak, M. Asle Zaeem, D. Moldovan, Combined molecular dynamics and phase field simulation investigations of crystal-melt interfacial properties and dendritic solidification of highly undercooled titanium, Computational Materials Science 163 (2019) 218-229.
[70] G. Azizi, S. Kavousi, M. Asle Zaeem, Interactive effects of interfacial energy anisotropy and solute transport on solidification patterns of Al-Cu alloys, Acta Materialia 231 (2022) 117859.
[71] W. Zhang, J. Smith, Nonstoichiometric interfaces and Al 2 O 3 adhesion with Al and Ag, Physical review letters 85(15) (2000) 3225.
[72] R. Yan, W.Z. Sun, S.D. Ma, T. Jing, H.B. Dong, The orientation dependence of liquid ordering at α-Al2O3/Al solid–liquid interfaces: A molecular dynamics study, Computational Materials Science 174 (2020) 109489.
[73] G. Pilania, B.J. Thijsse, R.G. Hoagland, I. Lazić, S.M. Valone, X.-Y. Liu, Revisiting the Al/Al2O3 Interface: Coherent Interfaces and Misfit Accommodation, Scientific Reports 4(1) (2014) 4485.
[74] A.J. Brown, H.B. Dong, P.B. Howes, C.L. Nicklin, In situ observation of the orientation relationship at the interface plane between substrate and nucleus using X-ray scattering techniques, Scripta Materialia 77 (2014) 60-63.
[75] Q. Zhang, A. van Duin, W. Goddard, W. Goddard, Y. Qi, L. Hector, Adhesion and nonwetting-wetting transition in the Al/α-Al2O3 interface, Physical Review B 69 (2004).
[76] G. Levi, W.D. Kaplan, Oxygen induced interfacial phenomena during wetting of alumina by liquid aluminium, Acta Materialia 50(1) (2002) 75-88.
[77] Q. Zhang, T. Çağın, A. van Duin, W.A. Goddard, Y. Qi, L.G. Hector, Adhesion and nonwetting-wetting transition in the $\mathrm{Al}/\ensuremath{\alpha}\ensuremath{-}{\mathrm{Al}}_{2}{\mathrm{O}}_{3}$ interface, Physical Review B 69(4) (2004) 045423.
[78] D.L. Medlin, K.F. McCarty, R.Q. Hwang, S.E. Guthrie, M.I. Baskes, Orientation relationships in heteroepitaxial aluminum films on sapphire, Thin Solid Films 299(1) (1997) 110-114.
[79] K. Han, J.P. Hirth, J.D. Embury, Modeling the formation of twins and stacking faults in the ag-cu system, Acta Materialia 49(9) (2001) 1537-1540.
[80] L. Zepeda-Ruiz, B. Sadigh, A. Chernov, T. Haxhimali, A. Samanta, T. Oppelstrup, S. Hamel, L. Benedict, J. Belof, Extraction of effective solid-liquid interfacial free energies for full 3D solid crystallites from equilibrium MD simulations, The Journal of Chemical Physics 147 (2017).
[81] F.J. Humphreys, M. Hatherly, Recrystallization and related annealing phenomena, Elsevier2012.
[82] G. Kaptay, On Surface Properties of Molten Aluminum Alloys of Oxidized Surface, Materials Science Forum - MATER SCI FORUM 77 (1991) 315-0.
[83] G.V. Samsonov, The oxide handbook, Springer Science & Business Media2013.
[84] S. Bao, K. Tang, A. Kvithyld, M. Tangstad, A. Engh, Wettability of Aluminum on Alumina, Metallurgical and Materials Transactions B 42 (2011) 1358-1366.
[85] H. John, H. Hausner, Influence of Oxygen Partial Pressure on Wetting Behavior in the System Al/Al2O3, Journal of Materials Science Letters 5 (1986) 549-551.
[86] D. Wang, s.-t. wu, The Influence of Oxidation on the Wettability of Aluminum on Sapphire, Acta Metallurgica et Materialia 42 (1994) 4029-4034.
[87] D.A. Porter, K.E. Easterling, Phase transformations in metals and alloys (revised reprint), CRC press2009.
[88] S. Mahajan, Critique of mechanisms of formation of deformation, annealing and growth twins: Face-centered cubic metals and alloys, Scripta Materialia 68(2) (2013) 95-99.
[89] P. Huang, G.Q. Dai, F. Wang, K.W. Xu, Y.H. Li, Fivefold annealing twin in nanocrystalline Cu, Applied Physics Letters 95(20) (2009) 203101.
[90] P. Parajuli, R. Mendoza-Cruz, J.J. Velazquez-Salazar, M.J. Yacaman, A. Ponce, Fivefold annealing twin in nanocrystalline Au/Pd film, Materials Letters 244 (2019) 88-91.

[91] Z. Deng, J. Luo, W. Yuan, W. Xi, Formation and disintegration investigation of fivefold annealing twins in copper nanoparticles, Scripta Materialia 169 (2019) 42-45.
[92] Y.T. Zhu, X.Z. Liao, R.Z. Valiev, Formation mechanism of fivefold deformation twins in nanocrystalline face-centered-cubic metals, Applied Physics Letters 86(10) (2005) 103112.
[93] E.M. Bringa, D. Farkas, A. Caro, Y.M. Wang, J. McNaney, R. Smith, Fivefold twin formation during annealing of nanocrystalline Cu, Scripta Materialia 59(12) (2008) 1267-1270.
[94] A.J. Cao, Y.G. Wei, Formation of fivefold deformation twins in nanocrystalline face-centered-cubic copper based on molecular dynamics simulations, Applied Physics Letters 89(4) (2006) 041919.
[95] M. Song, G. Zhou, N. Lu, J. Lee, E. Nakouzi, H. Wang, D. Li, Oriented attachment induces fivefold twins by forming and decomposing high-energy grain boundaries, Science 367(6473) (2020) 40-45.